Gross-Neveu Heisenberg criticality: Dynamical generation of quantum spin Hall masses

Yuhai Liu,[1] Zhenjiu Wang,[2] Toshihiro Sato,[2] Wenan Guo,[3,1,*] and Fakher F. Assaad[2,4,†]
[1]*Beijing Computational Science Research Center, Beijing 100193, China*
[2]*Institut für Theoretische Physik und Astrophysik, Universität Würzburg, Am Hubland, 97074 Würzburg, Germany*
[3]*Department of Physics, Beijing Normal University, Beijing 100875, China*
[4]*Würzburg-Dresden Cluster of Excellence ct.qmat, Am Hubland, 97074 Würzburg, Germany*

(Received 27 March 2021; revised 6 June 2021; accepted 17 June 2021; published 6 July 2021)

We consider fermions on a honeycomb lattice supplemented by a spin invariant interaction that dynamically generates a quantum spin Hall insulator. This lattice model provides an instance of Gross-Neveu Heisenberg criticality, as realized for example by the Hubbard model on the honeycomb lattice. Using auxiliary field quantum Monte Carlo simulations we show that we can compute with unprecedented precision susceptibilities of the order parameter. In O(N) Gross-Neveu transitions, the anomalous dimension of the bosonic mode grows as a function of N such that in the *large-N* limit it is of particular importance to consider susceptibilities rather than equal-time correlations so as to minimize contributions from the background. For the $N = 3$ case, we obtain $1/\nu = 1.11(4)$, $\eta_\phi = 0.80(9)$, and $\eta_\psi = 0.29(2)$, respectively, for the correlation length exponent, and the bosonic and fermionic anomalous dimensions.

DOI: 10.1103/PhysRevB.104.035107

I. INTRODUCTION

Fermionic quantum criticality is a long-standing problem in the domain of strongly correlated electron systems [1,2]. In d-wave superconductors [3,4] or in freestanding graphene [5–7] the problem greatly simplifies. Here, the Fermi surface consists of a discrete set of points with a linear dispersion relation at low energies that can be captured by a Dirac equation [8]. Fermion criticality in these systems refers to a set of phenomena such as the opening of a single particle gap [9] (mass generation), or nematic transitions where a Dirac point meanders [10,11].

In mass generating transitions in two spatial dimensions, one expects emergent Lorentz symmetry [12]. The field theory corresponds to Dirac fermions supplemented by a Yukawa term consisting of a Dirac mass [13] coupled to a bosonic mode described by a ϕ^4 theory [9]. At the Wilson-Fisher fixed point, the Yukawa coupling is relevant and drives the system to a new so-called Gross-Neveu (GN) critical point. In comparison to Wilson-Fisher fixed points where the bosonic anomalous dimension is small [14–16], fermion quantum criticality in Dirac systems is characterized by a much larger one. This can be understood intuitively since coupling to fermions provides new decay channels for bosonic modes. As noted in [7], this characteristic of the GN critical points potentially poses a numerical challenge. If in two spatial dimensions, the anomalous dimension of the bosonic mode is greater than unity, then the equal-time correlations of this mode will be dominated by the background. On the other hand, critical fluctuations will become apparent in the susceptibility. In principle this should not cause a problem since within auxiliary field quantum Monte Carlo (AFQMC) methods [17–20] one can compute time displaced correlation functions and hence susceptibilities. To the best of our knowledge, it turns out that computing susceptibilities for Hubbard-type models in the vicinity of the critical point is very noisy, and is plagued by rare configurations with anomalous fluctuations. This inhibits a precise determination of this quantity and to date analyses of GN criticality in lattice systems [5–7,21–24] are based on equal-time correlations of the critical bosonic mode.

In Ref. [25], we have introduced a model with an SU(2) spin symmetry that shows a transition from a Dirac semimetal (DSM) to a quantum spin Hall (QSH) insulator. As conjectured in Ref. [9] this transition is expected to belong to the same universality class as that of the Hubbard model on the Honeycomb lattice. Remarkably, our AFQMC implementation presented in Ref. [25] does not suffer from the aforementioned anomalous fluctuations of the critical bosonic modes. We are hence in a position to compute the susceptibility and extract critical exponents using this quantity. The main result of paper reads

$$1/\nu = 1.11(4), \ \eta_\phi = 0.80(9), \ \text{and} \ \eta_\psi = 0.29(2) \quad (1)$$

for the exponents of the $(2+1)$-dimensional GN-Heisenberg universality class at $N_f = 2$ four-component fermion fields akin to graphene. Here ν is the correlation length exponent and η_ϕ (η_ψ) the bosonic (fermionic) anomalous dimension.

The paper is organized as follows. In the next section, we define the model and the AFQMC approach. In Sec. III, we discuss our QMC results using a crossing-point analysis based on the time displaced correlations. Adopting this analysis scheme, corrections to scaling are taken into account. In Sec. IV we compare our results to previous estimates and provide concluding remarks. We have included three appendices.

*waguo@bnu.edu.cn
†fakher.assaad@physik.uni-wuerzburg.de

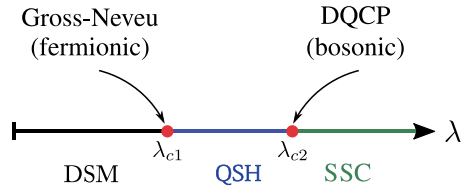

FIG. 1. Schematic ground-state phase diagram with DSM, QSH, and SSC phases. The DSM-QSH transition belongs to the Gross-Neveu Heisenberg universality class. The QSH-SSC is an example of a monopole-free deconfined quantum critical point (DQCP) [25].

In Appendix A we compare the quality of our susceptibility data to those of the generic Hubbard model on the honeycomb lattice. In Appendix B we provide a detailed symmetry based understanding of the single particle Green's function, which is used to compute the fermion anomalous dimension. Finally, in Appendix C we show that the correlation ratio is a renormalization group invariant quantity.

II. MODEL AND METHOD

We consider a honeycomb lattice model with Hamiltonian

$$\hat{H} = -t \sum_{\langle i,j\rangle} \hat{\boldsymbol{c}}_i^\dagger \hat{\boldsymbol{c}}_j - \lambda \sum_{\hexagon} \left(\sum_{\langle\langle ij\rangle\rangle \in \hexagon} \hat{\boldsymbol{J}}_{i,j} \right)^2,$$
$$\hat{\boldsymbol{J}}_{i,j} = i\nu_{ij} \hat{\boldsymbol{c}}_i^\dagger \boldsymbol{\sigma} \hat{\boldsymbol{c}}_j + \text{H.c.} \tag{2}$$

The spinor $\hat{\boldsymbol{c}}_i^\dagger = (\hat{c}_{i,\uparrow}^\dagger, \hat{c}_{i,\downarrow}^\dagger)$ where $\hat{c}_{i,\sigma}^\dagger$ creates an electron at lattice site $\boldsymbol{i}$ with z component of spin σ. The first term accounts for nearest-neighbor hopping. The second term is a hexagon interaction involving next-nearest-neighbor pairs of sites and phase factors $\nu_{ij} = -\nu_{ji} = \pm 1$ identical to those of the Kane-Mele model [26]. That is, assume that the honeycomb lattice spans the x-y plane, and let $\boldsymbol{r}$ be the nearest-neighbor site common to next-nearest-neighbor sites $\boldsymbol{i}$ and $\boldsymbol{j}$, then

$$\nu_{ij} = \text{sgn}[(\boldsymbol{i} - \boldsymbol{r}) \times (\boldsymbol{r} - \boldsymbol{j})] \cdot \boldsymbol{e}_z. \tag{3}$$

Finally, $\boldsymbol{\sigma} = (\sigma^x, \sigma^y, \sigma^z)$ corresponds to the vector of Pauli spin matrices. Since $\hat{\boldsymbol{J}}_{i,j}$ transforms as a vector under SU(2) spin rotations, the model possesses global SU(2) spin symmetry.

The ground state phase diagram as a function of λ presented in Ref. [25] is briefly summarized in Fig. 1. As a function of λ/t (we set $t = 1$), we observe three phases: a DSM for $\lambda < \lambda_{c1}$, a QSH insulator for $\lambda_{c1} < \lambda < \lambda_{c2}$, and an s-wave superconductor (SSC) at $\lambda > \lambda_{c2}$. The DSM and QSH states are separated by a Gross-Neveu Heisenberg phase transition at $\lambda_{c1} \approx 0.0187$; the QSH and SSC states are separated by a deconfined quantum critical point (DQCP) [27–29] at $\lambda_{c2} \approx 0.0332$. Here and in comparison to Ref. [25] we focus on the critical behavior of the Gross-Neveu Heisenberg transition. We simulated lattices with $L \times L$ unit cells ($N = 2L^2$ sites). Here we will provide results on larger lattice sites up to $N = 1152$ with $L = 24$ and determine the correlation length exponent, and bosonic and fermionic anomalous dimensions.

The model described by Hamiltonian (2) is investigated with the algorithms for lattice fermions (ALF) [30,31] implementation of finite temperature AFQMC [17–20]. Since the interaction is written in terms of squares of single body operators, it can be decomposed with a generic Hubbard-Stratonovich transformation [25,32,33]. We consider values of $\lambda > 0$ such that for a given instance of Hubbard-Stratonovitch fields, time reversal symmetry is present. This has the consequence that the eigenvalues of the fermion matrix occur in complex conjugate pairs [34]. Hence no sign problem occurs. Note that since adding a chemical potential does not break time reversal symmetry, finite dopings can also be considered [35]. For the details of the implementation of the algorithm, we refer the reader to Ref. [25]. In the following, we used $t = 1$ as the energy unit and simulated half-filled lattices with $L \times L$ unit cells with periodic boundary conditions. For the numerical simulations presented here, we have used a symmetric Trotter decomposition (see Ref. [31]) so as to ensure hermiticity of the imaginary time propagation. For the imaginary time step we have chosen, $\Delta_\tau = 0.2$ and as appropriate for Lorentz invariant systems have carried out an inverse temperature $\beta = L$ scaling analysis.

One key technical point of this study is that our specific implementation allows for the calculation of the order parameter susceptibility with unprecedented precision. In comparison to the Hubbard model on the honeycomb lattice, we show in Appendix A that we do not suffer from rare configurations with anomalous fluctuations when computing this quantity.

III. RESULTS

A. Order parameter

The DSM-QSH transition involves the breaking of an SU(2) spin rotation symmetry and is expected to be in the Gross-Neveu Heisenberg universality class for $N_f = 2$ four-component Dirac fermions (two sublattices, two Dirac cones, and spin $\sigma = \uparrow, \downarrow$). The local vector order parameter takes the form of the spin-orbit coupling,

$$\hat{\boldsymbol{O}}^{\text{QSH}}_{\boldsymbol{r},\langle\langle\boldsymbol{\delta},\boldsymbol{\delta}'\rangle\rangle} = i\hat{\boldsymbol{c}}^\dagger_{\boldsymbol{r},\boldsymbol{\delta}} \boldsymbol{\sigma} \hat{\boldsymbol{c}}_{\boldsymbol{r},\boldsymbol{\delta}'} + \text{H.c.}, \tag{4}$$

where $\boldsymbol{r}$ labels a unit cell or equivalently a hexagon, and $\langle\langle\boldsymbol{\delta}, \boldsymbol{\delta}'\rangle\rangle$ corresponds to next-nearest-neighbor pairs with legs $\boldsymbol{\delta}$ and $\boldsymbol{\delta}'$ of the corresponding hexagon. Because this order parameter is a lattice regularization of the three QSH mass terms in the Dirac equation [13], long-range order implies a mass gap. To study this phase transition, we use susceptibilities rather than equal-time correlations to suppress background contributions to the critical fluctuations. The associated time-displaced correlation functions of the spin-orbit coupling order parameter read

$$S^{\text{QSH}}_{\langle\langle\boldsymbol{\delta},\boldsymbol{\delta}'\rangle\rangle\langle\langle\boldsymbol{\delta}'',\boldsymbol{\delta}'''\rangle\rangle}(\boldsymbol{k},\tau) = \frac{1}{L^2} \sum_{\boldsymbol{r},\boldsymbol{r}'} \left\langle \hat{\boldsymbol{O}}^{\text{QSH}}_{\boldsymbol{r},\langle\langle\boldsymbol{\delta},\boldsymbol{\delta}'\rangle\rangle}(\tau) \cdot \hat{\boldsymbol{O}}^{\text{QSH}}_{\boldsymbol{r}',\langle\langle\boldsymbol{\delta}'',\boldsymbol{\delta}'''\rangle\rangle}(0) \right\rangle e^{i\boldsymbol{k}(\boldsymbol{r}-\boldsymbol{r}')}. \tag{5}$$

Here τ is the imaginary time. Since our model enjoys an SU(2) spin rotation symmetry and $\hat{\boldsymbol{O}}^{\text{QSH}}_{\boldsymbol{r},\langle\langle\boldsymbol{\delta},\boldsymbol{\delta}'\rangle\rangle}$ transforms as a vector under global rotations, we can neglect the background

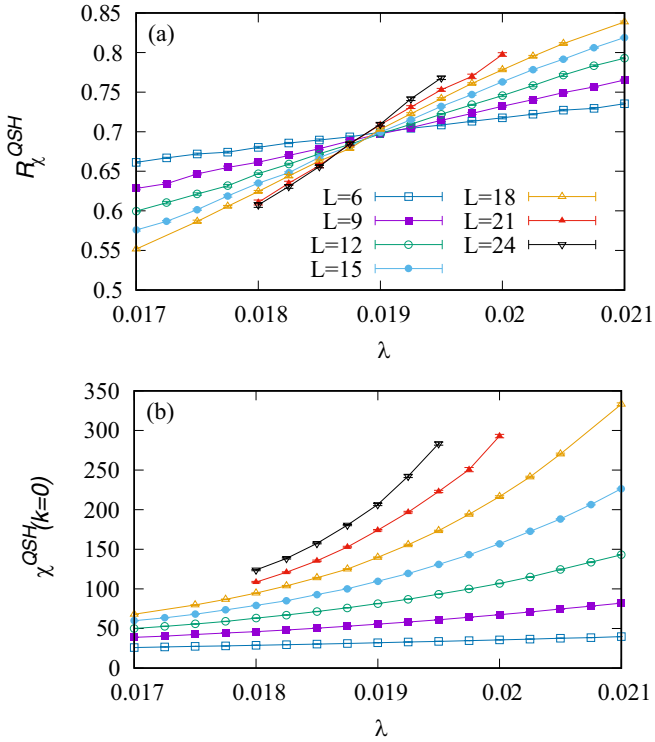

FIG. 2. (a) Correlation ratio and (b) susceptibility of the spin-orbit coupling order parameter for different system sizes across the DSM-QSH phase transition.

terms. We define the susceptibility as

$$\chi^{\mathrm{QSH}}(\boldsymbol{k}) = \Lambda_1\left(\int_0^\beta d\tau\, S^{\mathrm{QSH}}_{\langle\langle\boldsymbol{\delta},\boldsymbol{\delta}\rangle\rangle,\langle\langle\boldsymbol{\delta}'',\boldsymbol{\delta}'''\rangle\rangle}(\boldsymbol{k},\tau)\right), \tag{6}$$

where, $\Lambda_1()$ indicates the largest eigenvalue of the corresponding 6×6 matrix spanned by the $\langle\langle\boldsymbol{\delta},\boldsymbol{\delta}'\rangle\rangle$ and $\langle\langle\boldsymbol{\delta}'',\boldsymbol{\delta}'''\rangle\rangle$ indices corresponding to the six next-nearest-neighbor bonds of a hexagon. The QSH state is characterized by diverging $\chi^{\mathrm{QSH}}(\boldsymbol{k}=0)$. The corresponding renormalization-group invariant correlation ratio [36] (see Appendix C) reads

$$R_\chi^{\mathrm{QSH}} = 1 - \frac{\chi^{\mathrm{QSH}}(\boldsymbol{k}=\Delta\boldsymbol{k})}{\chi^{\mathrm{QSH}}(\boldsymbol{k}=0)}. \tag{7}$$

The ordering wave vector corresponds to $\boldsymbol{k}=0$, and on an $L\times L$ lattice with periodic boundary conditions, $|\Delta\boldsymbol{k}| = \frac{4\pi}{\sqrt{3}L}$. In the thermodynamic limit $R_\chi^{\mathrm{QSH}}\to 1$ ($R_\chi^{\mathrm{QSH}}\to 0$) in the ordered (disordered) phase and corresponds to a renormalization-group invariant quantity

$$R_\chi^{\mathrm{QSH}} = f_R[L^z/\beta, (\lambda-\lambda_c)L^{1/\nu}, L^{-w}], \tag{8}$$

at the critical point as discussed in Appendix C. Here β is the inverse temperature, z the dynamical critical exponent, ν the correlation length exponent, and ω the leading correction-to-scaling exponent. We will assume conformal invariance and set $z=1$ and $\beta=L$. Hence up to corrections to scaling, R_χ^{QSH} should show a crossing point at $\lambda=\lambda_c$. This is clearly seen in Fig. 2(a). In Fig. 2(b) we present the bare data, that support a divergence of the susceptibility beyond the crossing point of the correlation ratio. In particular, in the ordered phase, we expect the correlation length to diverge exponentially with

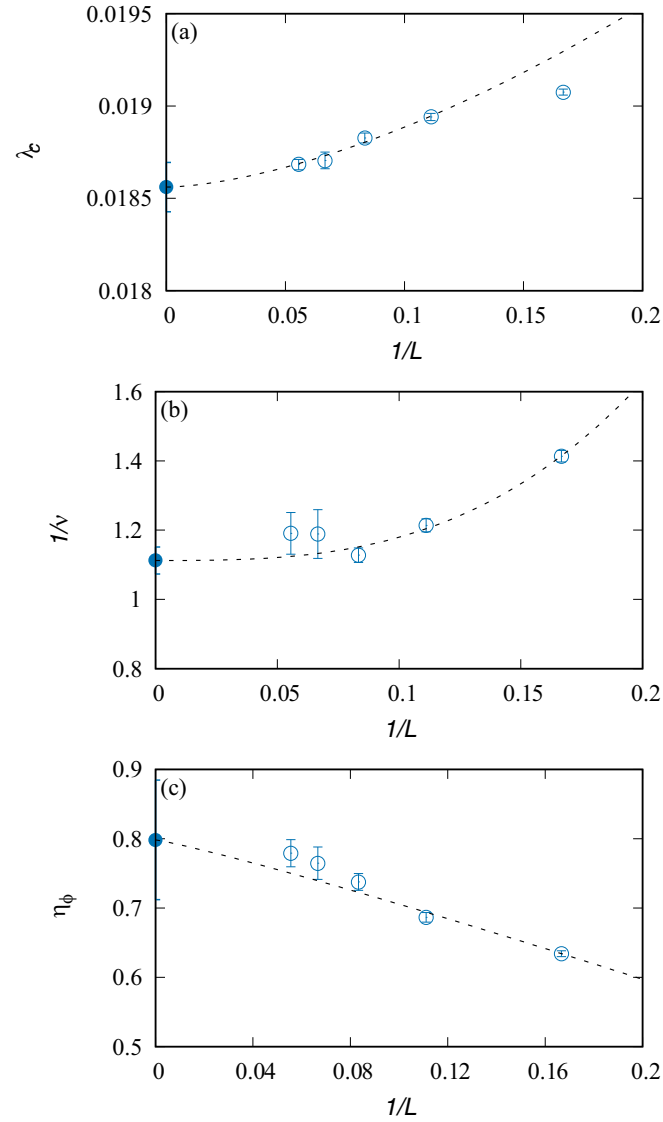

FIG. 3. (a) λ_c as a function of system size is obtained from a crossing-point analysis of the correlation ratio of Eq. (7) for L and $L+6$. (b) Correlation length exponent as a function of system size as obtained from Eq. (9). (c) Bosonic anomalous dimension as obtained from Eq. (11). From the fits (see text) we obtain $\lambda_c = 0.0186(2)$, $1/\nu = 1.11(4)$, and $\eta_\phi = 0.80(9)$ in the large system size limit.

inverse temperature [37]. For our $\beta = L$ scaling it will hence exceed the size of the system and we expect the susceptibility to scale as the Euclidean volume βL^2 in the large volume limit.

We locate the critical point with the crossing-point method. Aside from a polynomial interpolation of the data as a function of λ for each L, this analysis does not require any further fitting, and by definition, converges to the correct critical coupling with leading finite-size corrections given by $L^{-\omega-(1/\nu)}$. Figure 3(a) plots the finite-size estimate, $\lambda_c(L)$, corresponding to the crossing point of R_χ^{QSH} for L and $L+6$. Extrapolation to the thermodynamic limit yields $\lambda_c = 0.186(2)$ and $\lambda_c(L) = \lambda_c + a_1 L^{-\omega_1}$ with $\omega_1 = 1.6(5)$. Here ω_1, and also include ω_2, ω_3, and ω_4 corresponding to the correlation length exponent, and bosonic and fermionic anomalous dimensions,

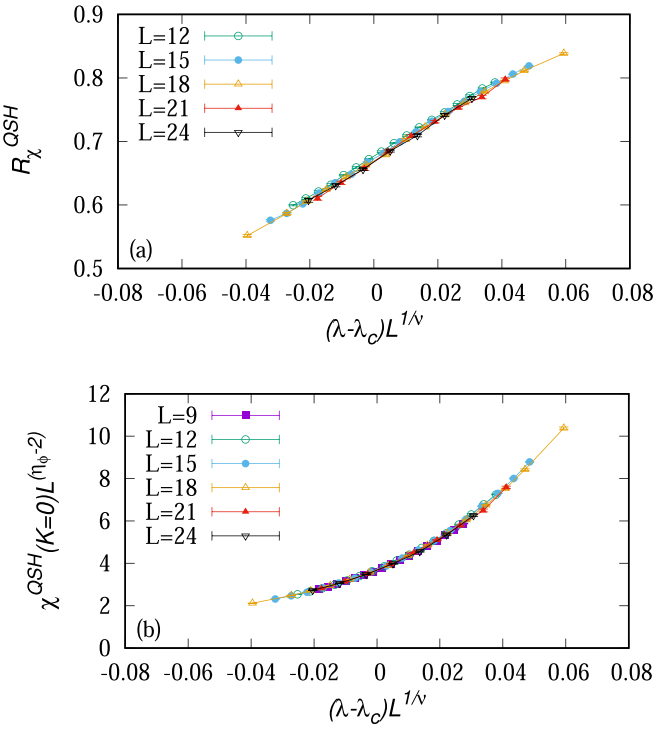

FIG. 4. As a cross-check for our determination of the critical point and exponents, we provide a data collapse with $\lambda_c = 0.0186$, $1/\nu = 1.11$, and $\eta_\phi = 0.8$ for (a) the correlation ratio and (b) the QSH susceptibility.

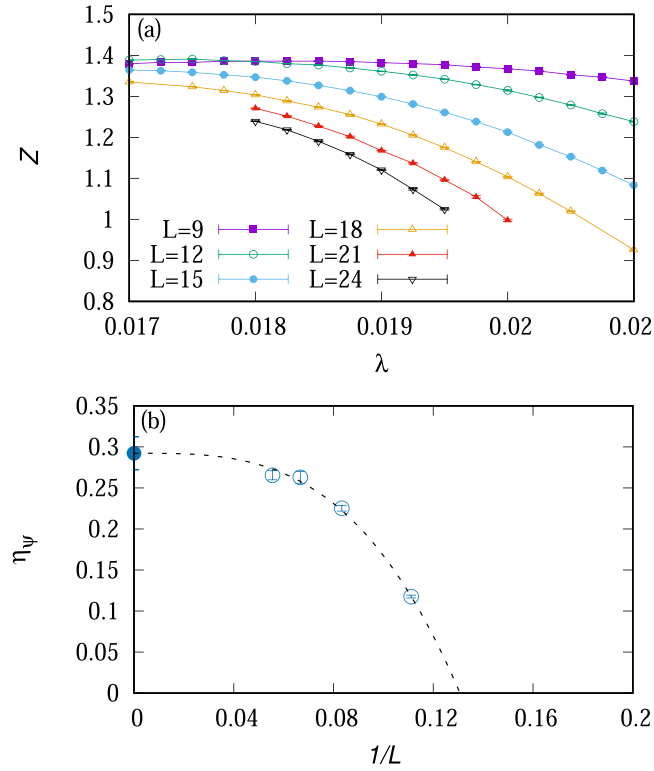

FIG. 5. (a) Monte Carlo estimate of Z as defined in Eq. (13). (a) Size scaling of the fermionic anomalous dimension as obtained from Eq. (15). In the large system size limit, we obtain $\eta_\psi = 0.29(2)$.

respectively, in the later part should be considered as "effective" exponents that change with the range of system sizes considered, which becomes the leading correction exponent only for very large sizes.

Based on Eq. (8) and the crossing-point analysis method in Ref. [38], we compute the correlation length exponent, ν, at crossing points of the correlation ratio via

$$\frac{1}{\nu^{\mathrm{QSH}}(L)} = \frac{1}{\ln(r)} \ln\left(\frac{\frac{d}{d\lambda}R_\chi^{\mathrm{QSH}}(\lambda, rL)}{\frac{d}{d\lambda}R_\chi^{\mathrm{QSH}}(\lambda, L)}\right)\Bigg|_{\lambda=\lambda_c(L)}. \quad (9)$$

Here $r = \frac{L}{L+6}$. The data of Fig. 3(b) supports $1/\nu = 1.11(4)$ and $1/\nu(L) = 1/\nu + b_1 L^{-\omega_2}$ with $\omega_2 = 2.9(8)$.

To estimate the bosonic anomalous dimension we consider the susceptibility

$$\chi^{\mathrm{QSH}}(\boldsymbol{k}=0) = L^{2-\eta_\phi} f_\chi[L^z/\beta, (\lambda-\lambda_c)L^{1/\nu}, L^{-w}], \quad (10)$$

at criticality such that

$$\eta_\phi(L, rL) = 2 - \frac{1}{\ln(r)} \ln\left(\frac{\chi^{\mathrm{QSH}}(\lambda_c(L), rL)}{\chi^{\mathrm{QSH}}(\lambda_c(L), L)}\right). \quad (11)$$

Again $r = \frac{L}{L+6}$, and $\lambda_c(L)$ refers to the size resolved crossing point of the correlation ratio. The data of Fig. 3(c) supports $\eta_\phi = 0.80(9)$ with $\eta_\phi(L) = \eta_\phi + c_1 L^{-\omega_3}$ and $\omega_3 = 1.4(6)$.

Finally, we check the critical point and exponents by collapsing the data on the basis of the finite-size scaling relations (8) and (10) without taking the correction to scaling terms ($L^{-\omega}$) into consideration. As expected and as shown in Figs. 4(a) and 4(b), the data for different system sizes collapse onto each other in the *large* size limit.

B. Single particle Green's functions

To extract the fermionic anomalous dimension, we consider the imaginary time displaced local single particle Green's function at $\tau = \beta/2 \equiv L/2$:

$$G(\lambda, L) = \frac{1}{2L^2} \sum_{\boldsymbol{r},\delta,\sigma} \langle \hat{c}^\dagger_{\boldsymbol{r}+\boldsymbol{\delta},\sigma}(\beta/2)\hat{c}_{\boldsymbol{r}+\boldsymbol{\delta},\sigma}(0)\rangle. \quad (12)$$

Here $\boldsymbol{r}$ denotes the unit cell, $\boldsymbol{\delta}$ is the orbital in the unit cell corresponding to the $A(B)$ sublattices, and σ is the spin degree of freedom. It is convenient to normalize $G(\lambda, L)$ with its noninteracting value so as to filter out size effects. This motivates the definition

$$Z = \frac{G(\lambda, L)}{G(0, L)}. \quad (13)$$

In the noninteracting case, $G(0, L)$ scales as L^{-2} reflecting the fermionic anomalous dimension, $d/2$ (d is the spatial dimension), of the fermion operator at the noninteracting fixed point (see Appendix B for a symmetry based discussion of the single particle Green's function).

In the vicinity of the GN critical point, we expect

$$Z = L^{-\eta_\psi} f_Z[L^z/\beta, (\lambda-\lambda_c)L^{1/\nu}, L^{-w}], \quad (14)$$

where η_ψ is the fermionic anomalous dimension. In Fig. 5(a) we report our bare data from which we can extract η_ψ using the relation

$$\eta_\psi(L, rL) = -\frac{1}{\ln(r)} \ln\left(\frac{Z(\lambda_c(L), rL)}{Z(\lambda_c(L), L)}\right) \quad (15)$$

with $r = \frac{L}{L+6}$, and $\lambda_c(L)$ the size resolved crossing points of the correlation ratio. In Fig. 5(b) we show that $\eta_\psi = 0.29(2)$ with $\eta_\psi(L) = \eta_\psi + d_1 L^{-\omega_4}$ and $\omega_4 = 3.2(6)$. We note that the single particle Green's function is not a Lorentz invariant quantity (see Appendix B). It is hence challenging to use the real space decay so as to extract the fermion anomalous dimension.

IV. DISCUSSIONS AND OUTLOOK

For $N_f = 2$ four-component Dirac fermions akin to graphene, there are a number of GN transitions that can be classified in terms of symmetry. After a canonical transformation, the noninteracting Dirac Hamiltonian of graphene is given by (see Appendix B)

$$\hat{H}_0 = -v_F \sum_{\boldsymbol{p}} \hat{\boldsymbol{\Psi}}^\dagger(\boldsymbol{p})[p_x \tau_x + p_y \tau_y]\hat{\boldsymbol{\Psi}}(\boldsymbol{p}), \tag{16}$$

where we label the eight-component spinor as $\hat{\boldsymbol{\Psi}}^\dagger := \Psi^\dagger_{\tau,\sigma,\mu}$. The $\tau_{x,y,z}$ Pauli matrices act on the τ indices and a similar notation holds for $\sigma_{x,y,z}$ and $\mu_{x,y,z}$ Pauli matrices. In this writing of the Dirac Hamiltonian, the SU(4) symmetry is explicit. $\hat{H}_0$ has a maximum of five mutually anticommuting mass terms corresponding to the matrices:

$$\boldsymbol{\Gamma} = (\boldsymbol{\sigma}\mu_x\tau_z, \mu_y\tau_z, \mu_z\tau_z). \tag{17}$$

The GN models

$$\hat{H}_N = \hat{H}_0 - U \sum_{i=1}^{N} \int_V d^2\boldsymbol{x}[\hat{\Psi}^\dagger(\boldsymbol{x})\Gamma_i\hat{\Psi}(\boldsymbol{x})]^2 \tag{18}$$

have O(N) symmetry, and the generators of the SO(N) subgroup are given by

$$\Gamma_{ij} = \frac{i}{4}[\Gamma_i, \Gamma_j], \quad i > j, \tag{19}$$

where $i \in 1 \ldots N$. The authors of Ref. [39] compute within an ϵ expansion around three spatial dimensions, as well as with functional renormalization group (FRG) methods the exponents for the aforementioned O(N)-GN transitions. In the FRG approximation, the bosonic anomalous dimensions read $\eta_\phi = 0.760, 0.875, 1.015, 1.159$, and $\eta_\phi = 1.285$ at $N = 1, 2, 3, 4, 5$, respectively. Hence, as N grows it becomes increasingly important to compute susceptibilities rather than equal-time correlation functions. Lattice regularizations of the above continuum theories can capture the O(1) or Z_2 [23], O(2) [40,41], as well as the O(3) [4–7] critical points. While Landau level regularization schemes allow one to simulate higher symmetries [42,43], O(4) and O(5) Gross-Neveu transitions seem to be realized only at multicritical points [39,44,45]. Such multicritical points have been put forward in fermion lattice models in Refs. [46,47] and Ref. [48] for the O(4) and O(5) cases respectively. Aside for the necessity of considering susceptibilities to investigate criticality, the task becomes especially challenging since one has to control two model parameters to locate the critical point.

In Hubbard based models, generically used to capture GN O(3) criticality, computing the susceptibilities of the bosonic mode turns out to be difficult due to anomalous fluctuations that suggest fat tailed distributions. When computing observables in the AFQMC, we divide by the fermion determinant [20]. The zeros of this quantity could be at the origin of these anomalous fluctuations. This interpretation has been put forward in Ref. [53]. It certainly may be part of the problem, but does not seem to provide an understanding of why the spin-susceptibility shows anomalous fluctuations but not, for instance, the charge susceptibility or the single particle time displaced correlation function. We refer the reader to Appendix A for further discussions and examples.

TABLE I. Comparison of critical exponents of the $N_f = 2$ four-component Dirac fermions Gross-Neveu O(3) critical point in 2+1 dimensions. The table is adapted from Ref. [22].

	$1/\nu$	η_ϕ	η_ψ
This study	1.11(4)	0.80(9)	0.29(2)
Ref. [4] (AFQMC)	0.95(5)	0.75(4)	0.23(4)
Ref. [49] (HMC)	0.861	0.872(22)	
Ref. [25] (AFQMC)	1.14(9)	0.79(5)	
Ref. [6] (AFQMC)	0.98(1)	0.49(2)	0.20(2)
Ref. [7] (AFQMC)	1.19(6)	0.70(15)	
Ref. [50] $(4-\epsilon)$, ϵ^4, Padé [2/2]	0.6426	0.9985	0.1833
Ref. [50] $(4-\epsilon)$, ϵ^4, Padé [3/1]	0.6447	0.9563	0.1560
Ref. [51] FRG	0.795	1.032	0.071
Ref. [52] FRG	0.76	1.01	0.08

We have noticed empirically that the AFQMC implementation of the model of Eq. (2) [25] showing a GN O(3) transition from a DSM to a QSH insulator does not suffer from the aforementioned issue. It hence provides a unique possibility to compute the exponents by considering susceptibilities rather than equal-time correlations. Our results are at best summarized by comparing with other calculations listed in Table I. The Monte Carlo results are ordered chronologically and convergence between different groups is apparent. In particular, the most recent independent calculations of Ref. [4], where the Dirac metal originates form a d-wave superconducting BCS state and the antiferromagnetic mass terms are generated dynamically with a Hubbard U term, compare very favorably to our DSM to QSH transition.

To progress in our determination of the critical exponents, high precision simulations on larger system sizes are desirable. In AFQMC algorithms, the fermion determinant is computed exactly such that the computational time per sweep for $\beta = L$ scaling reads L^7. Alternatively, in hybrid Monte Carlo (HMC) approaches [54,55] one generically evaluates the fermion determinant stochastically such that one can, in the ideal case, hope for an L^4 scaling corresponding to the Euclidean volume. In the vicinity of the GN critical point, such a scaling is not achievable, and the authors of Ref. [49] revert to an explicit calculation of the fermion determinant [56]. The origin for this poor scaling of the HMC, is the zeros of the fermion determinant. As mentioned above, one can conjecture that our ability to compute the order parameter susceptibilities stems from a low density of zeros of the fermion determinant. If so, it may be worthwhile to attempt HMC simulations of our model in the hope of reaching larger system sizes.

ACKNOWLEDGMENTS

We would like to thank Y. Otsuka, K. Seki, S. Sorella, F. Parisen Toldin, M. Ulybyshev, S. Yunoki and Disha Hou for valuable discussions. The authors gratefully acknowledge the Gauss Centre for Supercomputing e.V. for funding this project by providing computing time on the GCS Supercomputer SUPERMUC-NG at Leibniz Supercomputing Centre. F.F.A. acknowledges the Würzburg-Dresden Cluster of Excellence on Complexity and Topology in Quantum Matter ct.qmat (EXC 2147, Project ID 390858490). Z.W. acknowledges financial support from the DFG funded SFB 1170 on Topological and Correlated Electronics at Surfaces and Interfaces. T.S. acknowledges funding from the Deutsche Forschungsgemeinschaft under Grant No. SA 3986/1-1. Y.L. was supported by the China Postdoctoral Science Foundation under Grants No. 2019M660432 and No. 2020T130046 as well as the National Natural Science Foundation of China under Grants No. 11947232 and No.U1930402. W.G. was supported by the National Natural Science Foundation of China under Grants No. 11775021 and No. 11734002.

APPENDIX A: TIME DISPLACED CORRELATION FUNCTIONS

In this Appendix we present simulations for the Hubbard model on the honeycomb lattice close to the GN O(3) critical point. Our aim is to illustrate the difficulty in computing precisely the time displaced spin-spin correlations. In contrast the corresponding data for the model of Eq. (2) shows no such anomalous fluctuations up to $L = \beta = 24$.

Using the ALF-2.0 library [20,31], we can choose between different Hubbard-Stratonovich (HS) transformations: the field can couple to the density or to the magnetization [57]. The density decoupling is an SU(2) spin invariant code, meaning that for each field configuration, global SU(2) spin symmetry is present. On the other hand, coupling to the magnetization breaks the SU(2) symmetry to U(1). This symmetry will be restored after sampling over auxiliary field configurations. In Fig. 6 we plot the spin-spin correlations,

$$S(\boldsymbol{q}, \tau) = \frac{4}{3} \sum_{\delta} \sum_{\boldsymbol{r}} e^{i\boldsymbol{q}\cdot\boldsymbol{r}} \langle \boldsymbol{S}_{\boldsymbol{r},\delta}(\tau) \boldsymbol{S}_{\boldsymbol{0},\delta}(0) \rangle, \tag{A1}$$

where $\boldsymbol{r}$ denotes a unit cell, δ the orbital, and $\boldsymbol{S}_{\boldsymbol{r},\delta}$ is the spin operator. Here we consider an $L = 12$ lattice at $\beta t = 12$. As apparent, and within error bars, both HS transformations yield identical results. To assess the quality of the data we plot in Fig. 7 the single particle Green's function:

$$G(\boldsymbol{k}, \tau) = \frac{1}{2} \sum_{\delta,\sigma} \langle \hat{c}_{\boldsymbol{k},\delta,\sigma}(\tau) \hat{c}^{\dagger}_{\boldsymbol{k},\delta,\sigma} \rangle \tag{A2}$$

for the same run that produced the data of Fig. 6. As apparent, the quality of the single particle Green's function is excellent in comparison to the time displaced spin correlations. The larger error bars observed in the spin channel stem from *rare* configurations with *anomalous* fluctuations. The values of each bin for the spin

$$\chi_s = \int_0^{\beta} d\tau \, S(\boldsymbol{q} = 0, \tau) \tag{A3}$$

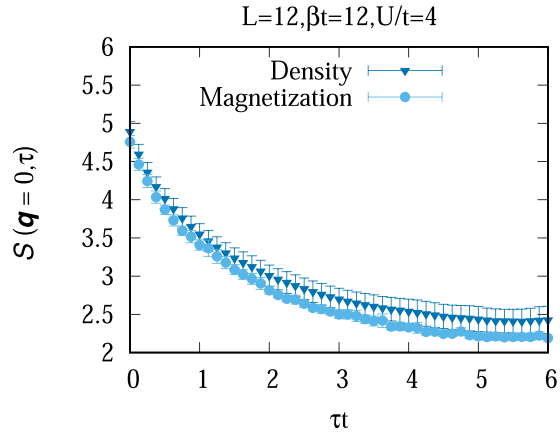

FIG. 6. Spin-spin time displaced correlation function at the ordering wave vector. Here we consider the Hubbard model on the honeycomb lattice in the proximity of the GN O(3) critical point. We present data for different choices of the HS transformation where the field couples to the density (triangles) or to the magnetization (circles).

and single particle

$$\chi_g = \int_0^{\beta} d\tau \, G(\boldsymbol{k} = 0, \tau) \tag{A4}$$

susceptibilities are plotted in Fig. 8. For the spin susceptibilities, one observes *spikes* in the bin values for both codes. On the other hand, the bin values of the Green's function susceptibility show no anomalies.

We now consider equivalent quantities albeit on much larger system sizes for the model of Eq. (2). In Fig. 9 we plot

$$S^{\mathrm{QSH}}(\boldsymbol{k}, \tau) = \sum_{\langle\langle \delta,\delta' \rangle\rangle} \sum_{\boldsymbol{r}} e^{i\boldsymbol{k}\cdot\boldsymbol{r}} \left\langle \hat{\boldsymbol{O}}^{\mathrm{QSH}}_{\boldsymbol{r},\langle\langle \delta,\delta' \rangle\rangle}(\tau) \cdot \hat{\boldsymbol{O}}^{\mathrm{QSH}}_{\boldsymbol{0},\langle\langle \delta,\delta' \rangle\rangle}(0) \right\rangle, \tag{A5}$$

where $\hat{\boldsymbol{O}}^{\mathrm{QSH}}_{\boldsymbol{r},\langle\langle \delta,\delta' \rangle\rangle}$ is defined in Eq. (4). As apparent, the data is of excellent quality.

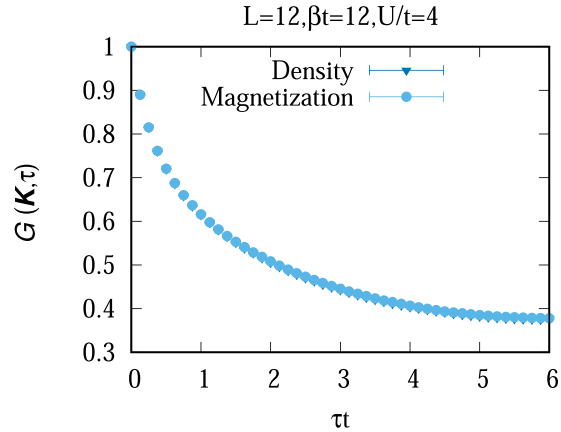

FIG. 7. Green's function at the Dirac point for the same run as in Fig. 6.

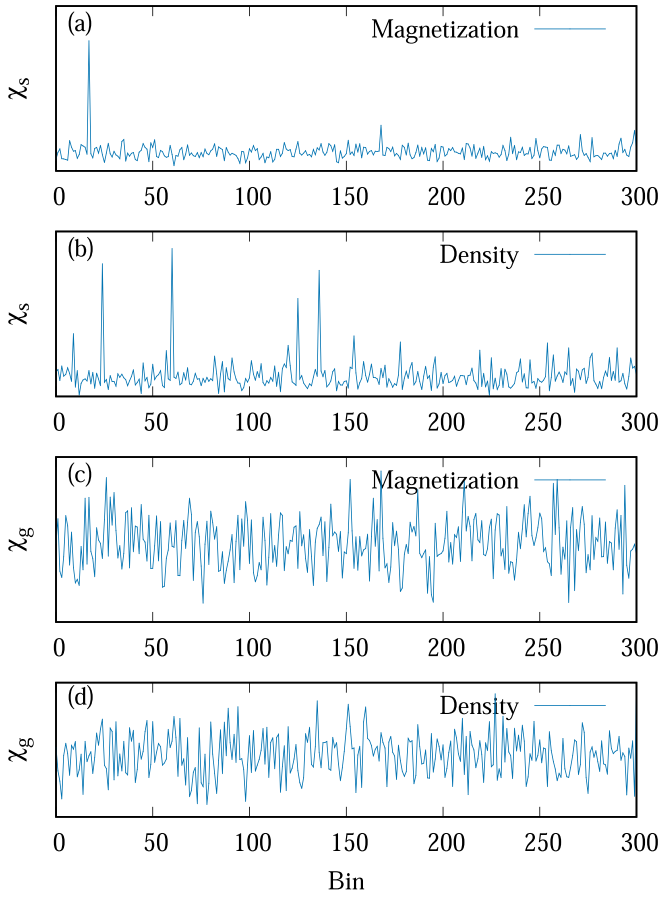

FIG. 8. Bin values for the spin (a),(b) and single particle (c),(d) susceptibilities for a 12×12 honeycomb lattice at $U/t = 4$ and $\beta t = 12$. (a),(c) The HS field couples to the magnetization. (b),(d) The HS field couples to the density. Each bin consists of 2400 sweeps.

In Fig. 10 we plot the local Green's function

$$G_{\text{local}}(\tau) = \frac{1}{2L^2} \sum_{\boldsymbol{r},\delta,\sigma} \langle \hat{c}^{\dagger}_{\boldsymbol{r}+\boldsymbol{\delta},\sigma}(\tau) \hat{c}_{\boldsymbol{r}+\boldsymbol{\delta},\sigma}(0) \rangle \tag{A6}$$

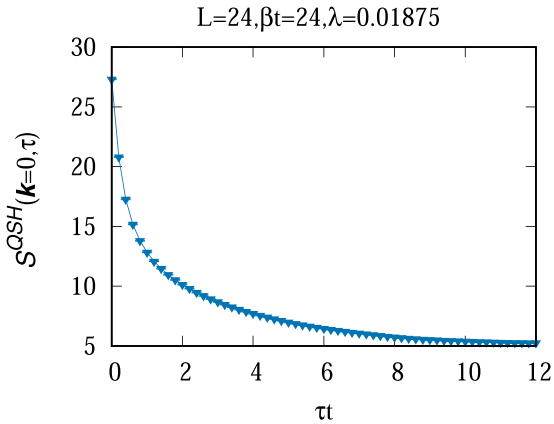

FIG. 9. Time displaced spin-orbit correlation functions at $L = \beta = 24$ and $\lambda = 0.018\,75$.

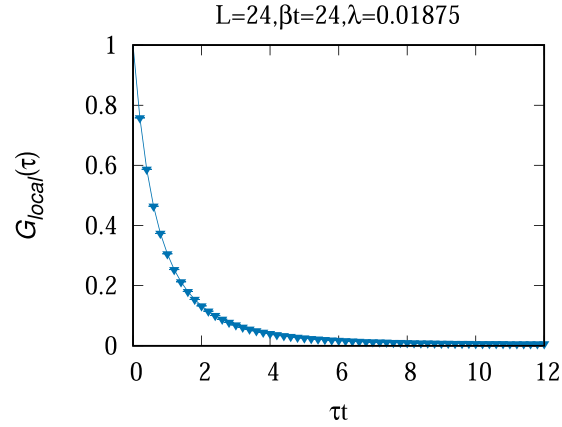

FIG. 10. Time displaced local Green's function for the same run as in Fig. 9.

used to obtain the fermion anomalous dimension. As apparent, the data quality is very good.

The spin-orbital coupling susceptibility reads

$$\chi^{\text{QSH}} = \Lambda_1 \left(\int_0^{\beta} d\tau \, S^{\text{QSH}}_{\langle\langle \boldsymbol{\delta},\boldsymbol{\delta}\rangle\rangle,\langle\langle \boldsymbol{\delta}'',\boldsymbol{\delta}'''\rangle\rangle}(\boldsymbol{k}=0,\tau) \right), \tag{A7}$$

where, $S^{\text{QSH}}_{\langle\langle \boldsymbol{\delta},\boldsymbol{\delta}\rangle\rangle,\langle\langle \boldsymbol{\delta}'',\boldsymbol{\delta}'''\rangle\rangle}$ is the time displaced correlation function of spin-orbit coupling order parameter and $\Lambda_1()$ indicates the largest eigenvalue of the 6×6 matrix spanned by the next-nearest-neighbor bonds of a hexagon. The values of each bin for χ^{QSH} and the three components χ^{QSH_x}, χ^{QSH_y}, and χ^{QSH_z} are plotted in Fig. 11. We observe no *spikes* in the bin values for all components.

APPENDIX B: SPACE AND TIME DEPENDENCE OF THE SINGLE PARTICLE GREEN'S FUNCTION

The aim of this appendix is to understand the behavior of the single particle Green's function in space and imaginary time using symmetry arguments. Let us start with the tight binding Hamiltonian on the honeycomb lattice that reads

$$\hat{H}_0 = -t \sum_{\boldsymbol{k}\in BZ} (\hat{a}^{\dagger}_{\boldsymbol{k}}, \hat{b}^{\dagger}_{\boldsymbol{k}}) \begin{pmatrix} 0 & Z(\boldsymbol{k}) \\ \overline{Z(\boldsymbol{k})} & 0 \end{pmatrix} \begin{pmatrix} \hat{a}_{\boldsymbol{k}} \\ \hat{b}_{\boldsymbol{k}} \end{pmatrix}. \tag{B1}$$

Here,

$$\hat{a}^{\dagger}_{\boldsymbol{k}} = \frac{1}{\sqrt{N}} \sum_{\boldsymbol{r}} e^{i\boldsymbol{k}\cdot\boldsymbol{r}} \hat{a}^{\dagger}_{\boldsymbol{r}} \tag{B2}$$

creates a Bloch state on orbital a of the unit cell. A similar equation holds for the b orbital. $\boldsymbol{r} = n\boldsymbol{a}_1 + m\boldsymbol{a}_2$ with $\boldsymbol{a}_1 = a(1,0)$, $\boldsymbol{a}_2 = a(\frac{1}{2}, \frac{\sqrt{3}}{2})$, and $n, m \in \mathbb{Z}$ runs over the unit cells. We have used periodic boundary conditions and

$$Z(\boldsymbol{k}) = 1 + e^{-i\boldsymbol{k}\cdot\boldsymbol{a}_2} + e^{-i\boldsymbol{k}\cdot(\boldsymbol{a}_2-\boldsymbol{a}_1)}. \tag{B3}$$

The Dirac points are defined by the zeros of $Z(\boldsymbol{k})$ and are located at

$$\boldsymbol{k} = \pm\boldsymbol{K}, \quad \text{with} \quad \boldsymbol{K} = \tfrac{4}{3}\boldsymbol{b}_1 + \tfrac{2}{3}\boldsymbol{b}_2 \tag{B4}$$

with $\boldsymbol{b}_i \cdot \boldsymbol{a}_j = 2\pi\delta_{i,j}$.

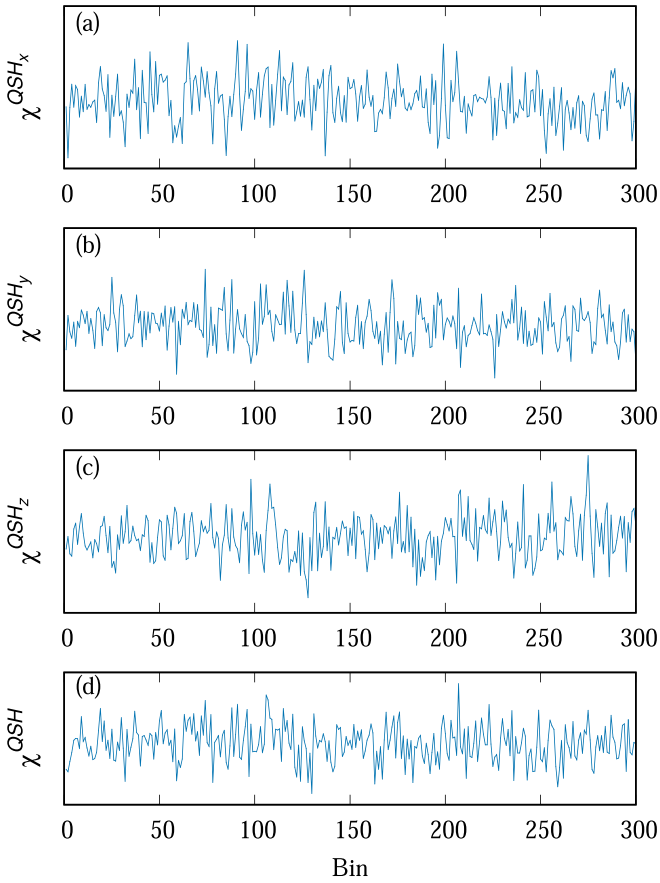

FIG. 11. Bin values for spin-orbital coupling susceptibility χ^{QSH} (d) and its three components χ^{QSH_x} (a), χ^{QSH_y}(b), and χ^{QSH_z}(c) for a 12×12 honeycomb lattice at $\lambda/t = 0.0186$ and $\beta t = 12$. Each bin consists of 2400 sweeps.

The Hamiltonian is invariant under the antiunitary particle-hole transformation

$$\hat{T}^{-1}\alpha\begin{pmatrix}\hat{a}^\dagger_{\boldsymbol{r}}\\ \hat{b}^\dagger_{\boldsymbol{r}}\end{pmatrix}\hat{T} = \overline{\alpha}\begin{pmatrix}\hat{b}_{\boldsymbol{r}}\\ -\hat{a}_{\boldsymbol{r}}\end{pmatrix} \tag{B5}$$

as well as under inversion symmetry,

$$\hat{I}^{-1}\begin{pmatrix}\hat{a}^\dagger_{\boldsymbol{r}}\\ \hat{b}^\dagger_{\boldsymbol{r}}\end{pmatrix}\hat{I} = \begin{pmatrix}\hat{b}^\dagger_{-\boldsymbol{r}}\\ \hat{a}^\dagger_{-\boldsymbol{r}}\end{pmatrix}. \tag{B6}$$

Hence, for $\boldsymbol{r} \neq \boldsymbol{0}$,

$$\begin{aligned}\langle \hat{a}^\dagger_{\boldsymbol{r}}\hat{a}_{\boldsymbol{0}}\rangle &= \langle \hat{b}_{\boldsymbol{r}}\hat{b}^\dagger_{\boldsymbol{0}}\rangle = -\langle \hat{b}^\dagger_{\boldsymbol{0}}\hat{b}_{\boldsymbol{r}}\rangle\\ &= -\langle \hat{b}^\dagger_{-\boldsymbol{r}}\hat{b}_{\boldsymbol{0}}\rangle = -\langle \hat{a}^\dagger_{\boldsymbol{r}}\hat{a}_{\boldsymbol{0}}\rangle\end{aligned} \tag{B7}$$

and $\langle \hat{a}^\dagger_{\boldsymbol{r}}\hat{a}_{\boldsymbol{0}}\rangle$ vanishes. In the last two steps, we have used translation and inversion symmetry. Similarly, one will show that $\langle \hat{b}^\dagger_{\boldsymbol{r}}\hat{b}_{\boldsymbol{0}}\rangle = 0$ again for $\boldsymbol{r} \neq \boldsymbol{0}$. Hence, provided that the symmetries of the Dirac Hamiltonian are not broken, only equal-time correlations between different orbitals do not vanish.

We will now show that there is no nonvanishing Lorentz invariant fermion bilinear such that we cannot expect a *simple* asymptotic behavior of the one particle propagator. Since Lorentz symmetry is emergent, we will consider the continuum limit by expanding around the Dirac points:

$$\begin{aligned}Z(\boldsymbol{K}+\boldsymbol{p}) &= \frac{\sqrt{3}a}{2}(p_x - ip_y),\\ Z(-\boldsymbol{K}+\boldsymbol{p}) &= -\frac{\sqrt{3}a}{2}(p_x + ip_y),\end{aligned} \tag{B8}$$

to obtain

$$\hat{H} = -v_F \sum_{\boldsymbol{p},i=1,2} \hat{\boldsymbol{c}}^\dagger_{\boldsymbol{p}} i p_i \gamma_0\gamma_i \hat{\boldsymbol{c}}_{\boldsymbol{p}}. \tag{B9}$$

Here $\hat{\boldsymbol{c}}^\dagger_{\boldsymbol{p}} \equiv \hat{c}^\dagger_{\boldsymbol{p},\mu=\pm\boldsymbol{K},\tau=a,b}$ such that $\hat{c}^\dagger_{\boldsymbol{p},\mu=\pm\boldsymbol{K},\tau=a} = \hat{a}^\dagger_{\pm\boldsymbol{K}+\boldsymbol{p}}$ and $\hat{c}^\dagger_{\boldsymbol{p},\mu=\pm\boldsymbol{K},\tau=b} = \hat{b}^\dagger_{\pm\boldsymbol{K}+\boldsymbol{p}}$. The Fermi velocity is given by $v_F = \frac{\sqrt{3}at}{2}$ and the γ matrices are defined as

$$\gamma_0 = \tau_z,\ \gamma_1 = \mu_z\tau_y,\ \gamma_2 = \tau_x,\ \gamma_3 = \mu_x\tau_y,\ \gamma_5 = \mu_y\tau_y. \tag{B10}$$

$\boldsymbol{\tau}$ and $\boldsymbol{\mu}$ are vectors of Pauli spin matrices that act on orbital and valley indices, respectively. As apparent, the γ matrices satisfy the Clifford algebra,

$$\{\gamma_\mu, \gamma_\nu\} = 2\delta_{\mu,\nu}. \tag{B11}$$

Note that the canonical transformation that leads to Eq. (16) is given by

$$\hat{\boldsymbol{c}}^\dagger = \hat{\Psi}^\dagger(\tau_y P_+ + P_-) \quad \text{with} \quad P_\pm = \tfrac{1}{2}(1 \pm \mu_z). \tag{B12}$$

With

$$\hat{\boldsymbol{c}}^\dagger_{\boldsymbol{p}} = \frac{1}{\sqrt{V}}\int_V d^2\boldsymbol{x}\, e^{i\boldsymbol{p}\cdot\boldsymbol{x}}\hat{\boldsymbol{c}}^\dagger(\boldsymbol{x}), \tag{B13}$$

the Euclidean time action is then given by

$$S = v_F \int d^2\boldsymbol{x}\, d\tau \sum_{\mu=0,2} \overline{\boldsymbol{c}}(\boldsymbol{x})\partial_\mu\gamma_\mu \boldsymbol{c}(\boldsymbol{x}). \tag{B14}$$

In the above,

$$\overline{\boldsymbol{c}}(\boldsymbol{x}) = \boldsymbol{c}^\dagger(\boldsymbol{x})\gamma_0, \tag{B15}$$

$$\partial_0 = \frac{\partial}{v_F\partial\tau} \quad \text{and} \quad \partial_i = \frac{\partial}{\partial x_i}$$

and $\boldsymbol{c}_{\boldsymbol{p}}$ is a Grassmann spinor. The Dirac equation is scale invariant. In particular under the transformation $\boldsymbol{x}' = b\boldsymbol{x}$ and $\tau' = b\tau$ the Euclidean action remains form invariant provided that the fermion fields transform as

$$\boldsymbol{c}'(\boldsymbol{x}') = b^{-d/2}\boldsymbol{c}(\boldsymbol{x}) \tag{B16}$$

for the two, $d = 2$, dimensional case. Hence, fermion bilinears can take the form

$$\begin{aligned}\langle \overline{\boldsymbol{c}}(x) M \boldsymbol{c}(0)\rangle \propto \frac{a}{(v_F\tau)^2} + \frac{b}{|\boldsymbol{x}|^2} + \frac{cx_1}{|\boldsymbol{x}|^3} + \frac{dx_2}{|\boldsymbol{x}|^3}\\ + \frac{a_L}{(v_F\tau)^2 + |\boldsymbol{x}|^2}\cdots.\end{aligned} \tag{B17}$$

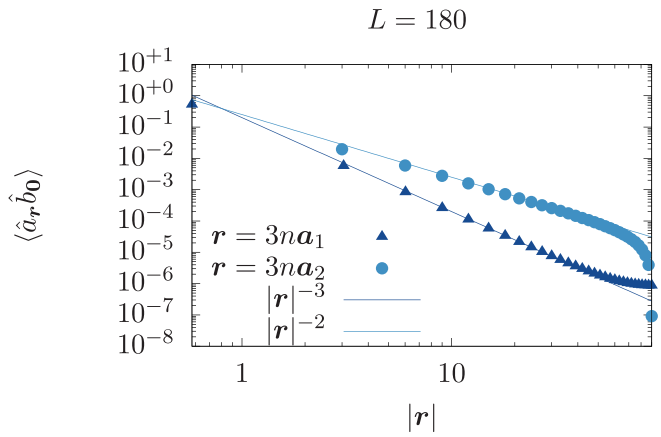

FIG. 12. Real space equal-time Green's function at zero temperature along different directions.

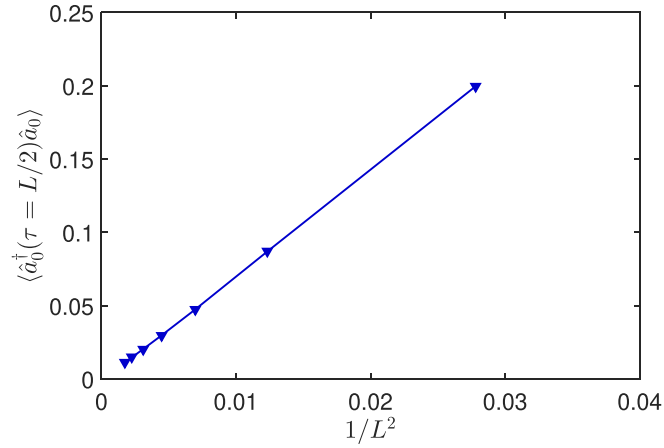

FIG. 13. Here we plot the time displaced local Green's function, at $\tau = \beta/2$ for $\beta = L$ simulations. As apparent, this quantity is proportional to L^{-2}.

The Dirac equation is Lorentz invariant [58] such that Lorentz invariant fermion bilinears scale as

$$\langle \bar{\boldsymbol{c}}(x) M_L \boldsymbol{c}(0) \rangle \propto \frac{a_L}{(v_F \tau)^2 + |\boldsymbol{x}|^2}. \tag{B18}$$

Examples of Lorentz invariant bilinears include

$$M_L = 1,\ M_L = i\gamma_3,\ M_L = i\gamma_5,\ M_L = i\gamma_3\gamma_5. \tag{B19}$$

These biliniears are mass terms corresponding respectively to charge-density wave (CDW) patterns, to the two Kékule orders, and finally to the Haldane mass. Since mass terms break symmetries of the Dirac Hamiltonian they vanish such that

$$\langle \bar{\boldsymbol{c}}(x) M_L \boldsymbol{c}(0) \rangle = 0. \tag{B20}$$

One can check the above explicitly for the CDW mass since it changes sign under inversion symmetry. We are hence left with fermion bilinears that are not Lorentz invariant, and hence do not enjoy rotational symmetry in space and imaginary time. In particular, computing $\langle \hat{a}_{\boldsymbol{r}}^\dagger \hat{b}_{\boldsymbol{0}} \rangle$ on the lattice amounts to considering $M = \gamma_0\gamma_2$. This is a nematic term that breaks Lorentz symmetry. An explicit calculation of the equal-time correlations of this fermion bilinear can be found in an Appendix of Ref. [59]. For distances on the lattice that satisfy $\boldsymbol{r} = n3\boldsymbol{a}_1 + m3\boldsymbol{a}_2$, $e^{\pm i\boldsymbol{K}\cdot\boldsymbol{r}} = 1$ and no oscillatory behavior is seen. In Fig. 12 we plot the equal-time Green's function using these sets of points. As apparent, depending upon the direction $1/r^2$ and $1/r^3$ decays are observed. Note that the $1/r^3$ decay can be justified by combining the terms $x_1/|\boldsymbol{x}|^3$ and $x_2/|\boldsymbol{x}|^3$ for $x_1 = x$ and $x_2 = a - x$.

Setting $\boldsymbol{x} = 0$ and considering solely imaginary time, greatly simplifies the analysis. In this case the scaling dimension of the fermion leads to

$$\langle \hat{a}_{\boldsymbol{0}}^\dagger(\tau) \hat{a}_{\boldsymbol{0}}(\tau = 0) \rangle \propto \frac{1}{(v_F \tau)^2}. \tag{B21}$$

In fact an explicit calculation of this quantity on the lattice and at zero temperature gives

$$\langle \hat{a}_{\boldsymbol{0}}^\dagger(\tau) \hat{a}_{\boldsymbol{0}}(\tau = 0) \rangle = \frac{1}{2N} \sum_{\boldsymbol{k}} e^{-\tau |tZ(\boldsymbol{k})|}. \tag{B22}$$

Expanding around the Dirac points, $Z(\pm\boldsymbol{K} + \boldsymbol{p}) = \frac{\sqrt{3}a}{2}|\boldsymbol{p}|$ and changing sums to integrals, yields the desired result. Figure 13 shows that adopting a $\beta = L$ scaling and considering $\tau = \beta/2$ provides confirmation of the above law.

At the Gross-Neveu critical point, the scaling dimension of the fermion operator will be enhanced by half the fermion anomalous dimension, η_Ψ, such that at this critical point we expect

$$\langle \hat{a}_{\boldsymbol{0}}^\dagger(\tau) \hat{a}_{\boldsymbol{0}}(\tau = 0) \rangle_{GN} \propto \frac{1}{(v_F \tau)^{2+\eta_\Psi}} \tag{B23}$$

in two spatial dimensions.

APPENDIX C: SCALING OF CORRELATION RATIO

Generically the space-time correlation function at a critical point with Lorentz invariance ($z = 1$) reads

$$C(\boldsymbol{r}, \tau, \xi, L, \beta) = (|\boldsymbol{r}|^2 + c^2\tau^2)^{-(D+z-2+\eta)/2} f\left(\frac{|\boldsymbol{r}|}{L}, \frac{\tau}{\beta}, \frac{\beta}{L}, \frac{\xi}{L}, L^{-\omega}\right), \tag{C1}$$

where ξ is the correlation length that depends on the distance from the critical point λ_c:

$$\xi \propto |\lambda - \lambda_c|^{-1/\nu}. \tag{C2}$$

Here we consider only one dominant scaling correction term with scaling dimension ω in Eq. (C1).

For a space $V \equiv L^D$ and imaginary time β volume, the susceptibility scales as

$$\begin{aligned}\chi(\boldsymbol{q}) &\equiv \int_0^\beta d\tau \int_{L^D} d^D\boldsymbol{r}\, C(\boldsymbol{r},\tau,\xi,L,\beta) e^{i\boldsymbol{q}\cdot\boldsymbol{r}} \\ &= \int_0^\beta d\tau \int_{L^D} d^D\boldsymbol{r} \left(|\boldsymbol{r}|^2 + c^2\tau^2\right)^{-(D+z-2+\eta)/2} f\left(\frac{|\boldsymbol{r}|}{L}, \frac{\tau}{\beta}, \frac{\beta}{L}, \frac{\xi}{L}, L^{-\omega}\right) e^{i\boldsymbol{q}\cdot\boldsymbol{r}} \\ &= \int_0^1 d\tau' \int_{1^D} d^D\boldsymbol{r}' \left(|\boldsymbol{r}'|^2 + \frac{\beta^2}{L^2} c^2 \tau'^2\right)^{-(D+z-2+\eta)/2} \frac{\beta}{L} L^{-(D+z-2+\eta)} L^{D+1} f\left(|\boldsymbol{r}'|, \tau', \frac{\beta}{L}, \frac{\xi}{L}, L^{-\omega}\right) e^{iL\boldsymbol{q}\cdot\boldsymbol{r}'} \\ &= F\left(\frac{\beta}{L}, \frac{\xi}{L}, L^{-\omega}, L|\boldsymbol{q}|\right) L^{2-\eta}. \end{aligned} \tag{C3}$$

In the second step, we carried out the variable substitutions, $\boldsymbol{r} = \boldsymbol{r}'L$ and $\tau = \beta\tau$. Hence the correlation ratio R scales as

$$\begin{aligned} R &\equiv 1 - \frac{L^{2-\eta} F\left(\frac{\beta}{L}, \frac{\xi}{L}, L^{-\omega}, L|\boldsymbol{q}_{\min}|\right)}{L^{2-\eta} F\left(\frac{\beta}{L}, \frac{\xi}{L}, L^{-\omega}, 0\right)} \\ &\equiv \widetilde{f}\left(\frac{\beta}{L}, \frac{\xi}{L}, L^{-\omega}\right) \\ &= f_R\left(\frac{\beta}{L}, L|\lambda - \lambda_c|^{1/\nu}, L^{-\omega}\right) \end{aligned} \tag{C4}$$

which stems from the fact that we fix $L|\boldsymbol{q}_{\min}|$ as a constant during finite-size scaling.

[1] J. A. Hertz, Phys. Rev. B **14**, 1165 (1976).
[2] A. J. Millis, Phys. Rev. B **48**, 7183 (1993).
[3] X. Y. Xu and T. Grover, Phys. Rev. Lett. **126**, 217002 (2021).
[4] Y. Otsuka, K. Seki, S. Sorella, and S. Yunoki, Phys. Rev. B **102**, 235105 (2020).
[5] F. F. Assaad and I. F. Herbut, Phys. Rev. X **3**, 031010 (2013).
[6] Y. Otsuka, S. Yunoki, and S. Sorella, Phys. Rev. X **6**, 011029 (2016).
[7] F. Parisen Toldin, M. Hohenadler, F. F. Assaad, and I. F. Herbut, Phys. Rev. B **91**, 165108 (2015).
[8] A. H. Castro Neto, F. Guinea, N. M. R. Peres, K. S. Novoselov, and A. K. Geim, Rev. Mod. Phys. **81**, 109 (2009).
[9] I. F. Herbut, V. Juričić, and O. Vafek, Phys. Rev. B **80**, 075432 (2009).
[10] M. Vojta, Y. Zhang, and S. Sachdev, Phys. Rev. Lett. **85**, 4940 (2000).
[11] E.-A. Kim, M. J. Lawler, P. Oreto, S. Sachdev, E. Fradkin, and S. A. Kivelson, Phys. Rev. B **77**, 184514 (2008).
[12] I. F. Herbut, V. Juričić, and B. Roy, Phys. Rev. B **79**, 085116 (2009).
[13] S. Ryu, C. Mudry, C.-Y. Hou, and C. Chamon, Phys. Rev. B **80**, 205319 (2009).
[14] M. Hasenbusch, Phys. Rev. B **82**, 174433 (2010).
[15] M. Campostrini, M. Hasenbusch, A. Pelissetto, P. Rossi, and E. Vicari, Phys. Rev. B **65**, 144520 (2002).
[16] F. Kos, D. Poland, D. Simmons-Duffin, and A. Vichi, J. High Energy Phys. 08 (2016) 036.
[17] R. Blankenbecler, D. J. Scalapino, and R. L. Sugar, Phys. Rev. D **24**, 2278 (1981).
[18] J. E. Hirsch, Phys. Rev. B **31**, 4403 (1985).
[19] S. R. White, D. J. Scalapino, R. L. Sugar, E. Y. Loh, J. E. Gubernatis, and R. T. Scalettar, Phys. Rev. B **40**, 506 (1989).
[20] F. Assaad and H. Evertz, in *Computational Many-Particle Physics*, edited by H. Fehske, R. Schneider, and A. Weiße, Lecture Notes in Physics Vol. 739 (Springer, Berlin/Heidelberg, 2008), pp. 277–356.
[21] T. C. Lang and A. M. Läuchli, Phys. Rev. Lett. **123**, 137602 (2019).
[22] E. Huffman and S. Chandrasekharan, Phys. Rev. D **101**, 074501 (2020).
[23] Y.-Y. He, X. Y. Xu, K. Sun, F. F. Assaad, Z. Y. Meng, and Z.-Y. Lu, Phys. Rev. B **97**, 081110(R) (2018).
[24] Y. Liu, W. Wang, K. Sun, and Z. Y. Meng, Phys. Rev. B **101**, 064308 (2020).
[25] Y. Liu, Z. Wang, T. Sato, M. Hohenadler, C. Wang, W. Guo, and F. F. Assaad, Nat. Commun. **10**, 2658 (2019).
[26] C. L. Kane and E. J. Mele, Phys. Rev. Lett. **95**, 226801 (2005).
[27] T. Senthil, L. Balents, S. Sachdev, A. Vishwanath, and M. P. A. Fisher, Phys. Rev. B **70**, 144407 (2004).
[28] T. Senthil, A. Vishwanath, L. Balents, S. Sachdev, and M. P. A. Fisher, Science **303**, 1490 (2004).
[29] T. Grover and T. Senthil, Phys. Rev. Lett. **100**, 156804 (2008).
[30] M. Bercx, F. Goth, J. S. Hofmann, and F. F. Assaad, SciPost Phys. **3**, 013 (2017).
[31] F. F. Assaad, M. Bercx, F. Goth, A. Götz, J. S. Hofmann, E. Huffman, Z. Liu, F. P. Toldin, J. S. E. Portela, and J. Schwab (ALF Collaboration), arXiv:2012.11914.
[32] Y. Motome and M. Imada, J. Phys. Soc. Jpn. **66**, 1872 (1997).
[33] F. F. Assaad, M. Imada, and D. J. Scalapino, Phys. Rev. B **56**, 15001 (1997).
[34] C. Wu and S.-C. Zhang, Phys. Rev. B **71**, 155115 (2005).
[35] Z. Wang, Y. Liu, T. Sato, M. Hohenadler, C. Wang, W. Guo, and F. F. Assaad, Phys. Rev. Lett. **126**, 205701 (2021).
[36] R. K. Kaul, Phys. Rev. Lett. **115**, 157202 (2015).

[37] S. Chakravarty, B. I. Halperin, and D. R. Nelson, Phys. Rev. Lett. **60**, 1057 (1988).
[38] H. Shao, W. Guo, and A. W. Sandvik, Science **352**, 213 (2016).
[39] L. Janssen, I. F. Herbut, and M. M. Scherer, Phys. Rev. B **97**, 041117(R) (2018).
[40] Z.-X. Li, Y.-F. Jiang, S.-K. Jian, and H. Yao, Nat. Commun. **8**, 314 (2017).
[41] Y. Otsuka, K. Seki, S. Sorella, and S. Yunoki, Phys. Rev. B **98**, 035126 (2018).
[42] M. Ippoliti, R. S. K. Mong, F. F. Assaad, and M. P. Zaletel, Phys. Rev. B **98**, 235108 (2018).
[43] Z. Wang, M. P. Zaletel, R. S. K. Mong, and F. F. Assaad, Phys. Rev. Lett. **126**, 045701 (2021).
[44] B. Roy and V. Juričić, Phys. Rev. B **99**, 241103 (2019).
[45] E. Torres, L. Weber, L. Janssen, S. Wessel, and M. M. Scherer, Phys. Rev. Research **2**, 022005(R) (2020).
[46] T. Sato, M. Hohenadler, and F. F. Assaad, Phys. Rev. Lett. **119**, 197203 (2017).
[47] T. Sato, M. Hohenadler, T. Grover, J. McGreevy, and F. F. Assaad, arXiv:2005.08996.
[48] Z.-X. Li, S.-K. Jian, and H. Yao, arXiv:1904.10975.
[49] P. Buividovich, D. Smith, M. Ulybyshev, and L. Von Smekal, Phys. Rev. B **98**, 235129 (2018).
[50] N. Zerf, L. N. Mihaila, P. Marquard, I. F. Herbut, and M. M. Scherer, Phys. Rev. D **96**, 096010 (2017).
[51] B. Knorr, Phys. Rev. B **97**, 075129 (2018).
[52] L. Janssen and I. F. Herbut, Phys. Rev. B **89**, 205403 (2014).
[53] H. Shi and S. Zhang, Phys. Rev. E **93**, 033303 (2016).
[54] S. Duane, A. D. Kennedy, B. J. Pendleton, and D. Roweth, Phys. Lett. B **195**, 216 (1987).
[55] S. Beyl, F. Goth, and F. F. Assaad, Phys. Rev. B **97**, 085144 (2018).
[56] M. Ulybyshev, N. Kintscher, K. Kahl, and P. Buividovich, Comput. Phys. Commun. **236**, 118 (2019).
[57] J. E. Hirsch, Phys. Rev. B **28**, 4059 (1983).
[58] M. E. Peskin and D. V. Schroeder, *An Introduction to Quantum Field Theory* (Westview, Boulder, CO, 1995), includes exercises.
[59] K. Seki, Y. Otsuka, S. Yunoki, and S. Sorella, Phys. Rev. B **99**, 125145 (2019).